

# Spin-orbit coupling controlled ground state in $\text{Sr}_2\text{ScOsO}_6$

A. E. Taylor,<sup>1</sup> R. Morrow,<sup>2</sup> R. S. Fishman,<sup>3</sup> S. Calder,<sup>1</sup> A.I. Kolesnikov,<sup>4</sup>  
M. D. Lumsden,<sup>1</sup> P. M. Woodward,<sup>2</sup> and A. D. Christianson<sup>1,5</sup>

<sup>1</sup>Quantum Condensed Matter Division, Oak Ridge National Laboratory, Oak Ridge, Tennessee 37831, USA

<sup>2</sup>Department of Chemistry, The Ohio State University, Columbus, Ohio 43210-1185, USA

<sup>3</sup>Materials Science and Technology Division, Oak Ridge National Laboratory, Oak Ridge, Tennessee 37831, USA

<sup>4</sup>Chemical and Engineering Materials Division, Oak Ridge National Laboratory, Oak Ridge, Tennessee 37831, USA

<sup>5</sup>Department of Physics and Astronomy, The University of Tennessee, Knoxville, TN 37996, USA

We report neutron scattering experiments which reveal a large spin gap in the magnetic excitation spectrum of  $\text{Sr}_2\text{ScOsO}_6$ . The spin-gap is demonstrative of appreciable spin-orbit-induced anisotropy, despite nominally orbitally-quenched  $5d^3$   $\text{Os}^{5+}$  ions. The system is successfully modeled with a Heisenberg Hamiltonian including exchange anisotropy, allowing the extraction of isotropic exchange parameters  $J_1$  and  $J_2$ . We find that the presence of the spin-orbit-induced anisotropy is essential for the realization of the type I antiferromagnetic ground state. This demonstrates that spin-orbit coupling plays an active role in determining the collective properties of  $4d^3$  and  $5d^3$  double perovskites.

The role of spin-orbit coupling (SOC) in  $4d$  and  $5d$  transition metal oxides is relatively poorly understood outside of the  $LS$  and  $JJ$  coupling limits. The need to understand the intermediate SOC regime is typified by the diverse range of properties found in double perovskites (DPs) containing  $4d$  and  $5d$  ions, including high-temperature half-metallic ferrimagnetism [1, 2], structurally selective magnetic states [3–5], complex geometric frustration [6–11], and Mott insulating ferromagnetism [12, 13]. Whilst this complex array of ground states has generated a great deal of interest, the interaction mechanisms controlling them remain undetermined.

For DP materials hosting  $4d^3$  and  $5d^3$  ions, the role of SOC is particularly unclear, and there exists dispute between different theories describing the  $d^3$  state and interactions [14, 15]. To first order,  $d^3$  ions in an octahedral environment are expected to be orbitally quenched, Fig. 1(a) [9, 16], yet there is mounting evidence that SOC has considerable influence [6, 11, 17–19]. This has been demonstrated by the presence of gaps of  $\sim 2$ – $18$  meV in the magnetic excitation spectra of  $\text{Ba}_2\text{YRuO}_6$ ,  $\text{La}_2\text{NaRuO}_6$  and  $\text{Ba}_2\text{YO}_6$  [9, 11, 17]. The presence of such large gaps, on the same energy scale as the  $T_N$ s, implies a departure from an orbital singlet, and raises questions over the role of SOC in the collective properties.

Beyond the fundamental interest in the influence of SOC, it is vital to determine the  $5d$  interactions in order to understand the wide variety of physical properties hosted by DPs, including the exceptionally high  $T_C = 725$  K discovered in  $\text{Sr}_2\text{CrOsO}_6$  [20, 21]. Investigations of  $\text{Sr}_2\text{CrOsO}_6$  and related materials indicate that the  $\text{Os}^{5+}$  ions play an essential role in the high transition temperature magnetism [3, 19, 22–26]. Determining the exchange interactions would allow the underlying behavior to be understood, and several attempts have been made to calculate these terms [22, 27–29]. However, experimentally obtaining the exchange terms is non-trivial,

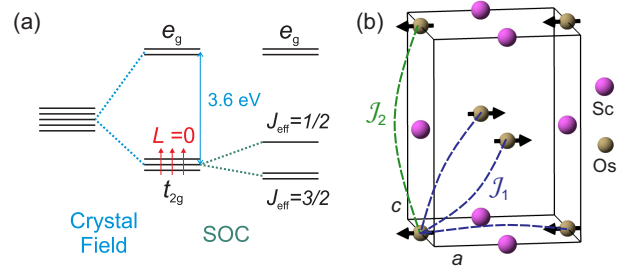


Figure 1. (a) Schematic of the energy levels for  $\text{Os}^{5+}$  in an octahedral environment.  $t_{2g}$ - $e_g$  splitting of 3.6 eV determined by x-ray absorption spectroscopy [30]. In the strong SOC limit the  $t_{2g}$  level can be further split into  $J_{\text{eff}} = \frac{1}{2}$  and  $\frac{3}{2}$  levels. Nominally the  $\text{Os}^{5+}$  ion is in the  $LS$  coupling limit and an  $L = 0$  state results. (b)  $\text{Sr}_2\text{ScOsO}_6$  magnetic structure, with moments depicted along  $a$ . One  $P2_1/n$  unit cell is shown, with O and Sr ions omitted for clarity. Dashed lines show examples of the NN ( $\times 12$ )  $J_1$  and NNN ( $\times 6$ )  $J_2$  exchanges.

and previous investigations have not achieved this.

To access the  $\text{Os}^{5+}$  interactions experimentally, we investigate  $\text{Sr}_2\text{ScOsO}_6$ . It is the single-magnetic-ion analogue of  $\text{Sr}_2\text{CrOsO}_6$ , therefore all magnetic interactions result solely from the frustrated quasi-face-centered-cubic lattice of  $\text{Os}^{5+}$  ions. Despite this,  $\text{Sr}_2\text{ScOsO}_6$  hosts a remarkably high  $T_N$  (92 K) for a single-magnetic-ion DP [19, 31, 32]. It is therefore a model system for investigating the role of the  $\text{Os}^{5+}$   $5d^3$  magnetic interactions in a high transition temperature material.

We present the inelastic neutron scattering (INS) spectrum of  $\text{Sr}_2\text{ScOsO}_6$ , and find a large spin gap below  $T_N$ . A Heisenberg Hamiltonian with anisotropic exchange terms is considered. We find that over a large parameter space, limited experimental constraints on the Hamiltonian enable the extraction of the nearest neighbor (NN),  $J_1$ , and next nearest neighbor (NNN),  $J_2$ , exchange terms. The success of the model reveals that

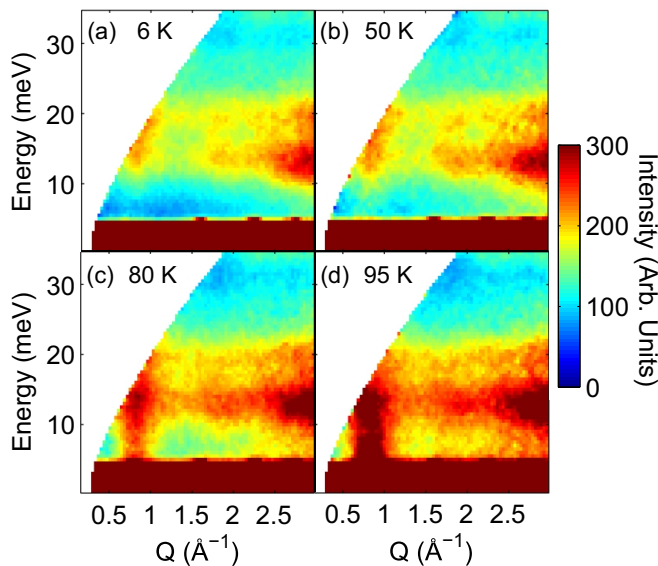


Figure 2. Neutron scattering intensity maps showing the evolution of the scattering from 95 K  $\approx T_N$ , to 80, 50 and 6 K  $< T_N$ , measured with  $E_i = 60$  meV.

SOC is essential to selection of the type I antiferromagnetic (AFM) ground state. This suggests that SOC, along with strong Os-O hybridization, promotes a high  $T_N$  in this otherwise frustrated material. Therefore, SOC within the  $5d^3$  manifold is key to the collective behavior realized in  $\text{Sr}_2\text{ScOsO}_6$ , and related  $4d^3$  and  $5d^3$  systems.

A 16.5 g polycrystalline sample of  $\text{Sr}_2\text{ScOsO}_6$  was used for INS experiments on SEQUOIA at the Spallation Neutron Source at Oak Ridge National Laboratory [33]. A portion of this sample was used to investigate the structural and magnetic properties as reported in Ref. [19]. Measurements were performed between 6 K and 115 K, using incident energies,  $E_i$ s, of 60 and 120 meV with chopper frequencies of 180 and 300 Hz, respectively. Empty Al-can measurements were subtracted from the data sets presented; raw  $\text{Sr}_2\text{ScOsO}_6$  and empty-can data are shown in the Supplemental Material (SM) [34].

The measured INS spectra at 6, 50, 80 and 95 K are shown in Fig. 2. There is a pronounced change in the spectrum at low neutron momentum transfer ( $Q$ ) upon crossing  $T_N = 92$  K. This behavior is reminiscent of the observed gap development below  $T_N$  in other single magnetic ion  $4d^3$  and  $5d^3$  DPs [9, 11, 17]. The higher  $Q$  scattering, which changes only in intensity with temperature, is identified as phonon scattering.

The detailed  $(Q, E)$ -space structure and temperature dependence of the scattering is presented in Fig. 3. Figure 3(a) demonstrates that intensity is distributed to higher energies at low temperatures, as expected from a gap opening. The peak of the scattering intensity at 6 K is  $\eta = 19(2)$  meV. This compares to previous observations, which have been used as a magnitude estimate

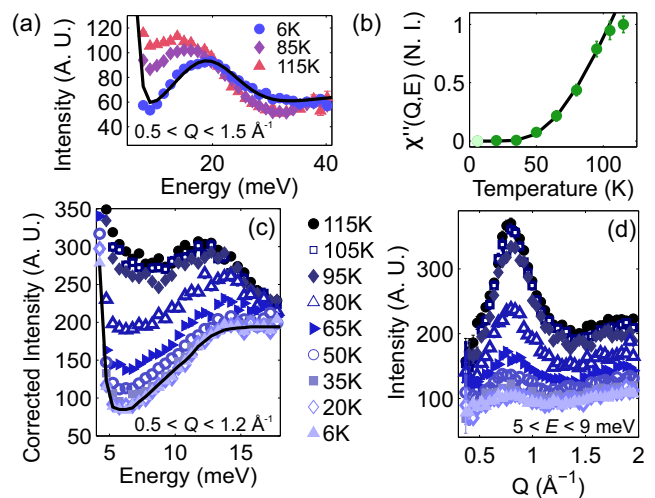


Figure 3. (a) Constant- $Q$  cuts from  $E_i = 120$  meV data. The solid line is the result of fitting Gaussians to the elastic line and to the inelastic magnetic signal at 6 K. A. U. stands for arbitrary units. (b)  $\chi''(T)$  at fixed  $Q$  and  $E$ , with an exponential,  $\chi''(T) \propto \exp(-\Delta/k_B T)$ , fit to the  $T < T_N$  data. N.I. stands for normalized intensity. (c) Constant- $Q$  cuts from  $E_i = 60$  meV data, which have been corrected for the Bose factor. Solid line is a guide to the eye. (d) Constant- $E$  cuts from  $E_i = 60$  meV data. In all panels errorbars are sometimes smaller than the symbols.

for the gap, of  $\eta = 18(2)$  meV in  $\text{Ba}_2\text{YOsO}_6$  ( $T_N = 69$  K),  $\eta \approx 5$  meV in  $\text{Ba}_2\text{YRuO}_6$  ( $T_N = 36$  K) and  $\eta \approx 2.75$  meV in  $\text{La}_2\text{NaRuO}_6$  ( $T_N = 15$  K) [9, 11, 17]. This generally supports a picture of gap-energy scale varying with  $T_N$ . Figure 3(c) presents data that has been corrected for the Bose thermal population factor,  $[1 - \exp(-E/k_B T)]^{-1}$ . The sharp drop in intensity at low  $E$  below  $T_N$  demonstrates the opening of the gap.

Figure 3(d) presents constant- $E$  cuts averaged from 5 to 9 meV. The scattering is centered around AFM ordering wavevector  $|\mathbf{Q}_{(001)}| \approx 0.8 \text{ \AA}^{-1}$ , with some asymmetry in the lineshape resulting from  $|\mathbf{Q}_{(100)/(010)}| \approx 1.1 \text{ \AA}^{-1}$  fluctuations. To track the relative strength of the fluctuations we extract the dynamic susceptibility,  $\chi''(T)$ , for fixed range  $5 < E < 9$  meV and  $0.5 < Q < 1.2 \text{ \AA}^{-1}$  via the same method as Ref. [11] (see also SM [34]). The opening of a gap below  $T_N$  is again indicated, Fig. 3(b), by the reduction in  $\chi''(T)$  at low-energy.

To reproduce the data, we investigate a model Heisenberg Hamiltonian. We parametrize the model with isotropic terms, the magnitude of which are decoupled from the physical origin of the spin gap, and exchange anisotropy terms to account for the gap. Unlike isotropic exchange terms, the anisotropic exchange terms only couple to a particular component of spin, e.g.  $S_x$ . We allow both NN and NNN interactions  $\mathcal{J}_1$  and  $\mathcal{J}_2$ , Fig. 1(b), to be anisotropic in spin space. We assume that the exchange interactions are unaffected by the weak non-

oclinic distortion, justified by two considerations: first, the size of the distortion is very small [19], much smaller than in systems in which the distortion rises to the level of affecting the physical properties [6]. Secondly, the properties of the closely related cubic compound  $\text{Ba}_2\text{YOsO}_6$  are exceptionally similar [11]. The Heisenberg exchanges are therefore written as

$$\begin{aligned}\mathcal{J}_{1\alpha\beta} &= J_1\delta_{\alpha\beta} + K_1\delta_{\alpha x}\delta_{\beta x} \\ \mathcal{J}_{2\alpha\beta} &= J_2\delta_{\alpha\beta} + K_2\delta_{\alpha x}\delta_{\beta x}.\end{aligned}$$

$J_1$ ,  $J_2$  and  $K_1$ ,  $K_2$  are the magnitudes of isotropic and anisotropic components, respectively, defined such that positive values are ferromagnetic (FM) and negative values are AFM.  $x$  represents the direction of spin alignment, which in crystallographic space is within the  $a$ - $b$  plane [19]. Since the model assumes that all 12 NN, and 6 NNN distances are equivalent, the real-space  $a$ - $b$  plane alignment of the spins does not affect the calculation. The exchange parameters scale inversely with spin,  $s$ . We use the Os moment determined from neutron diffraction,  $m = 1.6(1)\mu_B$  [19], giving  $s = 0.8$  [35].

Obtaining the exchange interactions allows the underlying behavior of a system to be understood, however doing so is non-trivial and previous investigations on similar systems have not achieved this. To accurately reproduce the INS data from  $\text{Sr}_2\text{ScOsO}_6$ , we first determine loose constraints on the parameter space. To accomplish this we solve for the four parameters  $J_1$ ,  $J_2$ ,  $K_1$ , and  $K_2$  based on four conditions. First, the ground state of the Os spins is the one depicted in Fig. 1(b). To confirm the ground state, we minimize the classical energy,  $\epsilon$ , among the 64 different spin configurations with distinct Os spins aligned along the  $\pm x$  directions in layers  $z = 0$ ,  $c/2$ ,  $c$ , and  $3c/2$ . Another stipulation for the local stability of the ground state is that the spin-wave frequencies are real throughout the magnetic Brillouin zone.

The second (third) condition is that the the bottom (top) of the spin-wave band is  $\Delta = 12$  meV ( $\Gamma = 40$  meV). The value of  $\Delta$  was selected by inspection of the 6 K data in Fig. 3(c), in which the increasing intensity begins to saturate at  $E \approx 12$  meV. The value of  $\Gamma$  was selected by inspection of broad constant- $Q$  cuts from the  $E_i = 120$  meV data sets (see SM Fig. S2 [34]), designed to capture all magnetic scattering up to high energies, in which 6 K and 115 K cuts converge at 40 meV. We tested alternative values of  $\Delta$  and  $\Gamma$ , and found that these did not reproduce the neutron scattering data, see SM [34]. We note that conditions two and three for  $\Delta$  and  $\Gamma$  are not independent, and that exchange anisotropies  $K_1$  and  $K_2$  have the same effect on the spin dynamics as a single anisotropy term  $\kappa = 3K_2 - 2K_1$ .

Finally, we apply a weak constraint using the  $T_N$  of 92 K. Calculated mean-field temperatures are generally expected to exceed the measured values [36], in our procedure it exceeds the measured  $T_N$  by a factor of two,

which is reasonable particularly given that the Curie-Weiss constant for this compound,  $\Theta = -677$  K [19], is far greater than 92 K. The conditions for the spin-wave energies  $\Delta$  and  $\Gamma$  are closely satisfied.

The parameters are calculated over a large range of  $K_1$  values. We find only two distinct branches of solutions, one with  $J_1 < 0$  and the other with  $J_1 > 0$ . We find ranges of possible solutions for  $J_1$ ,  $J_2$  and  $K_2$  for each  $K_1$ , even though  $\Delta$  and  $\Gamma$  depend only on the combination  $\kappa = 3K_2 - 2K_1$ , because the problem is under-determined [34]. For both branches, however, the average value for  $\kappa$  is constant over most of the range of  $K_1$  (Fig. S3 [34]). Note that  $\epsilon$  does not simply depend on  $\kappa$ .

Having determined the regions of parameter space which match our minimal constraints, we compare the simulated powder-averaged INS cross sections  $S(Q, E)$  to the low-temperature data, Fig. 4. The comparison tightly constrains the correct solutions out of the large parameter space searched. The branch of solutions with FM  $J_1 > 0$  fail to reproduce the observed data (see Fig. S4[34]). The  $S(Q, E)$  calculated with AFM  $J_1 < 0$ , however, qualitatively reproduce the 6 K data very well, Fig. 4. The comparison between calculation and  $E_i = 60$  meV data in Fig. 4(a) and (b) shows that the data are reproduced in the high-resolution configuration, but also indicates that accessing higher  $E$  and lower  $Q$  is desirable. This requires higher  $E_i$ , hence the equivalent calculation and  $E_i = 120$  meV data are shown in Fig. 4(c) and (d); the data are again very well reproduced. The loss of both experimental resolution and incident neutron flux limits the value of collecting data at higher  $E_i$ .

The simulations presented in Fig. 4 are for parameters  $K_1 = -3.2$  meV,  $J_1 = -4.1$  meV,  $J_2 = -2.2$  meV and  $K_2 = 2.0$  meV, as these are physically reasonable parameters for which  $J_1 > K_1$  and  $J_2 > K_2$ . Unique solutions for  $K_1$  and  $K_2$  cannot be found due to the constraints of modeling a polycrystalline data set, see SM for additional solutions [34], but the values of  $J_1$  and  $J_2$  are stable across the solutions. Therefore, the determined range of values  $J_1 = -3.6$  to  $-4.7$  meV and  $J_2 = -1.8$  to  $-2.3$  meV are a robust description of the experimental data, independent of the origin of the spin gap. The comparable magnitude of  $J_2$  to  $J_1$  highlights the significance of the extended Os  $5d$  orbitals. The determination that both  $J_1$  and  $J_2$  are AFM has significant implications for modeling the  $\text{Os}^{5+}$  DPs, as we discuss below.

Although SOC has been noted as the origin of the spin gap in 5d DPs [11, 17], the underlying mechanism by which it acts to produce the gap remains an open question. In general, the possible origins of such behavior in a three dimensional system are Dzyaloshinsky-Moriya (DM) interactions, single-ion anisotropy, and exchange anisotropy, all of which are induced by SOC. There are two observations which favor dismissal of the DM interaction as the origin of the gap: (i) the highly symmetric cubic or close-to-cubic crystal structures in which the gap

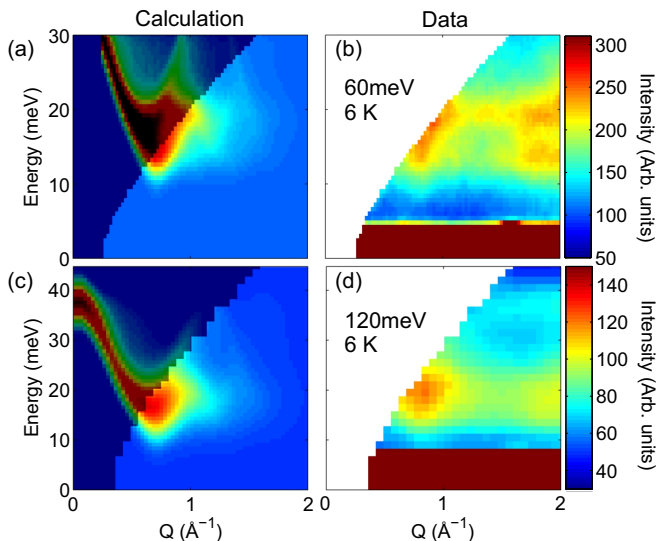


Figure 4. (a) and (c) Simulated spin-wave spectra, from calculated parameters  $K_1 = -3.2$  meV,  $J_1 = -4.1$  meV,  $J_2 = -2.2$  meV and  $K_2 = 2.0$  meV. Modeled using linear spin-wave theory [37], with powder averaging performed by sampling  $10^4$  random points in reciprocal space. Gaussian energy broadening is applied, as an approximation to instrument resolution, using 4 meV ((a)) and 6.8 meV ((c)), estimated from the full width at half maximum of the incoherent part of the elastic line in the data sets. The equivalent data sets collected at  $T = 6$  K with (b)  $E_i = 60$  meV and (d)  $E_i = 120$  meV are shown. The intensity at high  $Q$  in the data is due to phonon scattering, which is not included in the model. The shaded region in the calculations indicates the region of  $(Q, E)$  space which is inaccessible in the experiment.

has been observed [38] and (ii) the type I collinear AFM structure common to several DPs including  $\text{Sr}_2\text{ScOsO}_6$  – two perpendicular DM interactions would be required to produce a gap, but would favor a non-collinear spin state.

We also expect that single-ion anisotropy is negligible, because it is dramatically suppressed for the orbitally suppressed  $d^3$  configuration, and the 3.6 eV  $t_{2g}$  to  $e_g$  splitting in  $\text{Sr}_2\text{ScOsO}_6$  [30] means that the excited state perturbations are minimal [39]. This is supported by the experimental observation that no gap emerges in  $\text{La}_2\text{NaOsO}_6$  which only displays short-range order, whereas a gap is observed in long-ranged-ordered sister-compound  $\text{La}_2\text{NaRuO}_6$  [17]. A single-ion term, being a local effect, would not be sensitive to short- versus long-range order, and would emerge in the short-range ordered state. Therefore, exchange anisotropy is the most-likely explanation for the gap in  $4d^3$  and  $5d^3$  DPs. It has previously been discussed as the dominant term over single-ion effects for monoclinic  $5d^3$   $\text{Sr}_2\text{YRuO}_6$  [10].

Independent of the gap’s origin, the determination that  $J_1$  and  $J_2$  are both AFM has significant consequences. Type I AFM order is found in  $\text{Sr}_2\text{ScOsO}_6$ ,  $\text{Sr}_2\text{YRuO}_6$ ,  $\text{Ba}_2\text{YO}_6$  and  $\text{Ba}_2\text{YRuO}_6$ , but theoretical calculations

have found competition between type I and type III AFM order [10]. For an isotropic Heisenberg Hamiltonian, the ground state is type I only if  $J_1$  is AFM whilst  $J_2$  is FM. If both  $J_1$  and  $J_2$  are AFM, then some sort of anisotropy must be included for the ground state to be type I. Our results show that the latter mechanism is the origin of type I order in  $\text{Sr}_2\text{ScOsO}_6$ . Therefore, SOC is essential in determining the magnetic ground state.

As has previously been noted, large Os-O hybridization is an important factor in heightened  $T_N$ s in these DPs [19, 23]. Our results suggest that  $\text{Os}^{5+}$  SOC also acts to enhance  $T_N$  in  $\text{Sr}_2\text{ScOsO}_6$ . By promoting selection of a particular ground state, SOC assists in relieving the inherent frustration of the nearly-face-centered cubic lattice. This notion is supported by the trend in gap size with  $T_N$  across the measured compounds, and by the observation that  $3d$  transition metal DPs have lower  $T_N$ s and usually favor a different, Type II, ground state [40].

The results presented therefore highlight that SOC must be considered in  $4d^3$  and  $5d^3$  DPs. Previous attempts to model the exchange interactions in  $3d^x$ - $5d^3$  DPs, including  $\text{Sr}_2\text{CrOsO}_6$ , using density functional theory (DFT) have not considered anisotropy terms (single-ion or exchange anisotropy) [23, 27–29], but have mentioned the likely frustration of  $\text{Os}^{5+}$  ions. Therefore, for the mixed  $3d^x$ - $5d^3$  systems with high transition temperatures, a similar mechanism to that found for  $\text{Sr}_2\text{ScOsO}_6$  is likely to have influence. Our results will therefore stimulate further calculations which include anisotropy terms. For  $\text{Sr}_2\text{ScOsO}_6$  calculations will be constrained by the size of the observed gap and by the determined isotropic parameters, independent of the gap’s origin.

It is also informative to compare  $\text{Sr}_2\text{ScOsO}_6$  to the equivalent  $5d^2$  systems  $\text{Sr}_2\text{MgOsO}_6$  [32] and  $\text{Sr}_2\text{ScReO}_6$  [41, 42]. We expect  $5d^2$  ions to have a smaller magnetic moment [43], which results in lower energy scales, but unquenched SOC, which will promote a high  $T_N$  compared to that energy scale if the SOC promotion of  $T_N$  is correct. Both these expectations are met – compared to  $\text{Sr}_2\text{ScOsO}_6$  these compounds have lower inherent energy scales as indicated by their Curie Weiss constants, but despite this have  $T_N$ s of 105 K and 75 K, comparable to that of  $\text{Sr}_2\text{ScOsO}_6$ . Therefore SOC has an important role in high- $T_N$  DPs beyond the  $5d^3$  case.

In conclusion, by modeling the magnetic excitation spectrum of archetypal system  $\text{Sr}_2\text{ScOsO}_6$ , we have extracted the isotropic exchange parameters resulting from  $\text{Os}^{5+}$  ion interactions. The presence of a large spin gap demonstrates the significance of SOC, and the deviation of the  $5d^3$  ions from a nominal orbital singlet. As a consequence, SOC-induced anisotropy governs the magnetic state in this otherwise frustrated system, and assists in promoting a high  $T_N$ . This demonstrates that the role of anisotropy should be considered for the collective properties of high- $T_C$   $5d^3$  systems including  $\text{Sr}_2\text{CrOsO}_6$ .

The authors gratefully acknowledge M. Stone for useful

discussions. The research at Oak Ridge National Laboratory's Spallation Neutron Source was supported by the Scientific User Facilities Division, Office of Basic Energy Sciences, U.S. Department of Energy (DOE). Support for a portion of this research was provided by the Center for Emergent Materials an NSF Materials Research Science and Engineering Center (DMR-1420451). Research by RF sponsored by the DOE, Office of Science, Basic Energy Sciences, Materials Sciences and Engineering Division.

This manuscript has been authored by UT-Battelle, LLC under Contract No. DE-AC05-00OR22725 with the U.S. Department of Energy. The United States Government retains and the publisher, by accepting the article for publication, acknowledges that the United States Government retains a non-exclusive, paid-up, irrevocable, world-wide license to publish or reproduce the published form of this manuscript, or allow others to do so, for United States Government purposes. The Department of Energy will provide public access to these results of federally sponsored research in accordance with the DOE Public Access Plan (<http://energy.gov/downloads/doe-public-access-plan>)

- 
- [1] K.-I. Kobayashi, T. Kimura, H. Sawada, K. Terakura, and Y. Tokura, *Nature* **395**, 677 (1998).
- [2] K.-I. Kobayashi, T. Kimura, Y. Tomioka, H. Sawada, K. Terakura, and Y. Tokura, *Phys. Rev. B* **59**, 11159 (1999).
- [3] H. L. Feng, M. Arai, Y. Matsushita, Y. Tsujimoto, Y. Guo, C. I. Sathish, X. Wang, Y.-H. Yuan, M. Tanaka, and K. Yamaura, *J. Am. Chem. Soc.* (2014).
- [4] R. Morrow, J. W. Freeland, and P. M. Woodward, *Inorg. Chem.* **53**, 7983 (2014).
- [5] R. Morrow, J. Yan, M. A. McGuire, J. W. Freeland, D. Haskel, and P. M. Woodward, *Phys. Rev. B* **92**, 094435 (2015).
- [6] A. A. Aczel, D. E. Bugaris, L. Li, J.-Q. Yan, C. de la Cruz, H.-C. zur Loye, and S. E. Nagler, *Phys. Rev. B* **87**, 014435 (2013).
- [7] T. Aharen, J. E. Greedan, F. Ning, T. Imai, V. Michaelis, S. Kroeker, H. Zhou, C. R. Wiebe, and L. M. D. Cran-  
swick, *Phys. Rev. B* **80**, 134423 (2009).
- [8] P. L. Bernardo, L. Ghivelder, H. S. Amorim, J. J. Neumeier, and S. Garcia, *arXiv:1509.04377* (2015).
- [9] J. P. Carlo, J. P. Clancy, K. Fritsch, C. A. Marjerrison, G. E. Granroth, J. E. Greedan, H. A. Dabkowska, and B. D. Gaulin, *Phys. Rev. B* **88**, 024418 (2013).
- [10] E. V. Kuz'min, S. G. Ovchinnikov, and D. J. Singh, *Phys. Rev. B* **68**, 024409 (2003).
- [11] E. Kermarrec, C. A. Marjerrison, C. M. Thompson, D. D. Maharaj, K. Levin, S. Kroeker, G. E. Granroth, R. Flacau, Z. Yamani, J. E. Greedan, and B. D. Gaulin, *Phys. Rev. B* **91**, 075133 (2015).
- [12] A. S. Erickson, S. Misra, G. J. Miller, R. R. Gupta, Z. Schlesinger, W. A. Harrison, J. M. Kim, and I. R. Fisher, *Phys. Rev. Lett.* **99**, 016404 (2007).
- [13] S. Gangopadhyay and W. E. Pickett, *Phys. Rev. B* **91**, 045133 (2015).
- [14] S. Middey, A. K. Nandy, S. K. Pandey, P. Mahadevan, and D. D. Sarma, *Phys. Rev. B* **86**, 104406 (2012).
- [15] H. Matsuura and K. Miyake, *J. Phys. Soc. Jpn.* **82**, 073703 (2013).
- [16] G. Chen and L. Balents, *Phys. Rev. B* **84**, 094420 (2011).
- [17] A. A. Aczel, P. J. Baker, D. E. Bugaris, J. Yeon, H.-C. zur Loye, T. Guidi, and D. T. Adroja, *Phys. Rev. Lett.* **112**, 117603 (2014).
- [18] G. J. Nilsen, C. M. Thompson, G. Ehlers, C. A. Marjerrison, and J. E. Greedan, *Phys. Rev. B* **91**, 054415 (2015).
- [19] A. E. Taylor, R. Morrow, D. J. Singh, S. Calder, M. D. Lumsden, P. M. Woodward, and A. D. Christianson, *Phys. Rev. B* **91**, 100406 (2015).
- [20] Y. Krockenberger, M. Reehuis, M. Tovar, K. Mogare, M. Jansen, and L. Alff, *Journal of Magnetism and Magnetic Materials* **310**, 1854 (2007).
- [21] Y. Krockenberger, K. Mogare, M. Reehuis, M. Tovar, M. Jansen, G. Vaitheeswaran, V. Kanchana, F. Bultmark, A. Delin, F. Wilhelm, A. Rogalev, A. Winkler, and L. Alff, *Phys. Rev. B* **75**, 020404 (2007).
- [22] O. N. Meetei, O. Erten, M. Randeria, N. Trivedi, and P. Woodward, *Phys. Rev. Lett.* **110**, 087203 (2013).
- [23] H. Das, P. Sanyal, T. Saha-Dasgupta, and D. D. Sarma, *Phys. Rev. B* **83**, 104418 (2011).
- [24] P. Sanyal, *Phys. Rev. B* **89**, 115129 (2014).
- [25] A. K. Paul, M. Reehuis, V. Ksenofontov, B. Yan, A. Hoser, D. M. Többens, P. M. Abdala, P. Adler, M. Jansen, and C. Felser, *Phys. Rev. Lett.* **111**, 167205 (2013).
- [26] K. Samanta, P. Sanyal, and T. Saha-Dasgupta, *Scientific Reports* **5**, 15010 (2015).
- [27] S. Kanungo, B. Yan, M. Jansen, and C. Felser, *Phys. Rev. B* **89**, 214414 (2014).
- [28] Y. S. Hou, H. J. Xiang, and X. G. Gong, *Scientific Reports* **5**, 13159 (2015).
- [29] J. Wang, N. Zu, X. Hao, Y. Xu, Z. Li, Z. Wu, and F. Gao, *Physica Status Solidi (RRL)* **08**, 776 (2014).
- [30] J.-H. Choy, D.-K. Kim, and J.-Y. Kim, *Solid State Ionics* **108**, 159 (1998).
- [31] A. K. Paul, A. Sarapulova, P. Adler, M. Reehuis, S. Kanungo, D. Mikhailova, W. Schnelle, Z. Hu, C. Kuo, V. Siruguri, S. Rayaprol, Y. Soo, B. Yan, C. Felser, L. Hao Tjeng, and M. Jansen, *Z. anorg. allg. Chem.* **641**, 197 (2015).
- [32] Y. Yuan, H. L. Feng, M. P. Ghimire, Y. Matsushita, Y. Tsujimoto, J. He, M. Tanaka, Y. Katsuya, and K. Yamaura, *Inorg. Chem.* (2015), 10.1021/ic503086a.
- [33] G. E. Granroth, A. I. Kolesnikov, T. E. Sherline, J. P. Clancy, K. A. Ross, J. P. C. Ruff, B. D. Gaulin, and S. E. Nagler, *J. Phys.: Conf. Ser.* **251**, 012058 (2010).
- [34] Supplementary material includes additional INS data and spin-wave model calculations.
- [35] Assuming a g-factor of 2, which is reasonable since the ratio of spin to orbital moments is  $\sim 15$  according to DFT [19].
- [36] D. C. Mattis, *The Theory of Magnetism* (Harper & Row, New York, 1965).
- [37] S. Toth and B. Lake, *J. Phys.: Condens. Matter* **27**, 166002 (2015).
- [38] Space group  $Fm\bar{3}m$  has inversion symmetry on the Os site,  $P2_1/n$  does not.

- [39] D. I. Khomskii, *Transition Metal Compounds*, 1st ed. (Cambridge University Press, Cambridge, 2014).
- [40] S. Vasala and M. Karppinen, *Progress in Solid State Chemistry* **43**, 1 (2015).
- [41] H. Kato, T. Okuda, Y. Okimoto, Y. Tomioka, K. Oikawa, T. Kamiyama, and Y. Tokura, *Phys. Rev. B* **69**, 184412 (2004).
- [42] A. Winkler, N. Narayanan, D. Mikhailova, K. G. Bramnik, H. Ehrenberg, H. Fuess, G. Vaitheeswaran, V. Kanchana, F. Wilhelm, A. Rogalev, A. Kolchinskaya, and L. Alff, *New J. Phys.* **11**, 073047 (2009).
- [43] C. M. Thompson, J. P. Carlo, R. Flacau, T. Aharen, I. A. Leahy, J. R. Pollicemi, T. J. S. Munsie, T. Medina, G. M. Luke, J. Munevar, S. Cheung, T. Goko, Y. J. Uemura, and J. E. Greedan, *J. Phys.: Condens. Matter* **26**, 306003 (2014).

# Supplementary information for: Spin-orbit coupling controlled ground state in $\text{Sr}_2\text{ScOsO}_6$

A. E. Taylor,<sup>1</sup> R. Morrow,<sup>2</sup> R. S. Fishman,<sup>3</sup> S. Calder,<sup>1</sup> A.I. Kolesnikov,<sup>4</sup>  
M. D. Lumsden,<sup>1</sup> P. M. Woodward,<sup>2</sup> and A. D. Christianson<sup>1,5</sup>

<sup>1</sup>Quantum Condensed Matter Division, Oak Ridge National Laboratory, Oak Ridge, Tennessee 37831, USA

<sup>2</sup>Department of Chemistry, The Ohio State University, Columbus, Ohio 43210-1185, USA

<sup>3</sup>Materials Science and Technology Division, Oak Ridge National Laboratory, Oak Ridge, Tennessee 37831, USA

<sup>4</sup>Chemical and Engineering Materials Division, Oak Ridge National Laboratory, Oak Ridge, Tennessee 37831, USA

<sup>5</sup>Department of Physics and Astronomy, The University of Tennessee, Knoxville, TN 37996, USA

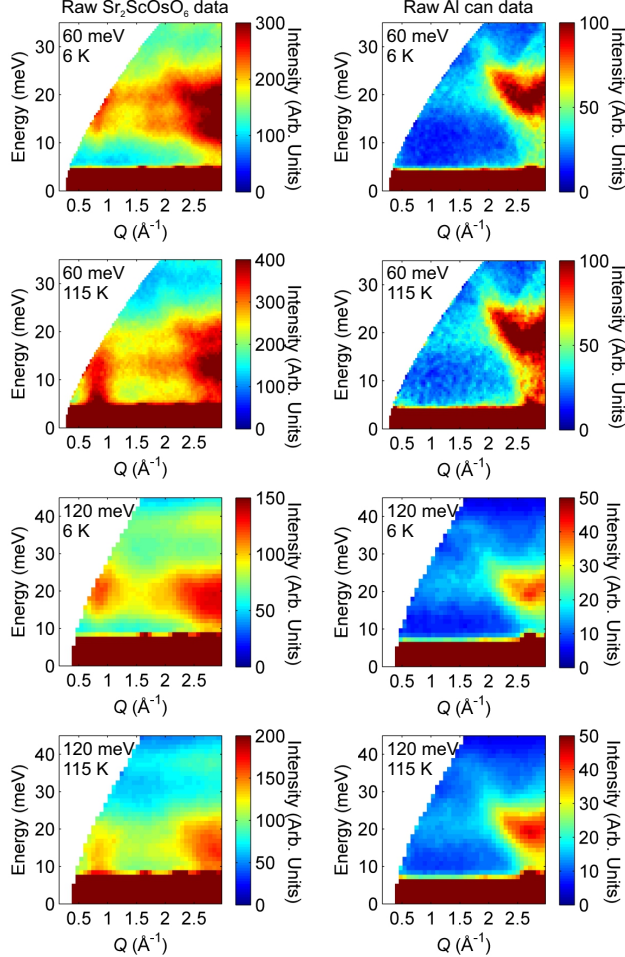


Figure S1. (Color online) Neutron scattering intensity maps showing the  $\text{Sr}_2\text{ScOsO}_6$  data before Al can subtraction and the raw Al can data, as indicated. Labels on each plot indicate the temperature and incident energy used in the measurements.

## INELASTIC NEUTRON SCATTERING

Here we present additional figures from the neutron scattering measurements on SEQUOIA. A closed-cycle refrigerator was used to access temperatures between 6 K and 115 K. The sample was sealed in a 4 mm-thick flat-

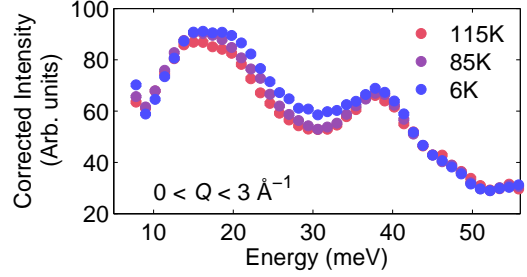


Figure S2. (Color online) Constant wavevector cuts averaged over a large low- $Q$  range, 0 to  $3 \text{ \AA}^{-1}$ . Data are from the  $E_i = 120 \text{ meV}$  SEQUOIA datasets measured on  $\text{Sr}_2\text{ScOsO}_6$  with equivalent background measurements of the empty Al can subtracted. Data has been corrected for the Bose thermal population factor.

plate Al can, and an identical empty can was measured as a background. Figure S1 shows raw data collected from  $\text{Sr}_2\text{ScOsO}_6$  prior to the empty can subtraction for temperatures above and below  $T_N$ . The equivalent raw data used for the empty can background subtraction are also shown, but presented on a lower intensity scale in order that features are visible. It is clear from comparing these intensity maps that the scattering attributed to magnetic fluctuations results from  $\text{Sr}_2\text{ScOsO}_6$ , and not a background feature.

In Fig. S2 we present constant wavevector cuts averaged over a large low- $Q$  range, 0 to  $3 \text{ \AA}^{-1}$ , in order to include all magnetic scattering and enable us to compare data between different temperatures up to high energies. These data have been corrected for the Bose factor to enable this comparison. The opening of the gap pushes intensity to higher energies in 85 K and 6 K datasets, but the 6 K data appears to converge with the other temperatures at  $E \approx 40 \text{ meV}$ , which we identify as  $\Gamma$  in the main text. There is a phonon mode present at  $E \approx 38 \text{ meV}$  but its position remains constant with temperature.

The  $\chi''(Q, E)$  data presented in Fig. 3(b) was calculated as follows, similar to the method described in Kermarrec *et al.* [23]. The integrated intensity of the  $E_i = 60 \text{ meV}$  data between  $5 < E < 9 \text{ meV}$  and  $0.5 < Q < 1.2 \text{ \AA}^{-1}$  was found at each temperature, then the 6 K data is used as a background. The Bose factor

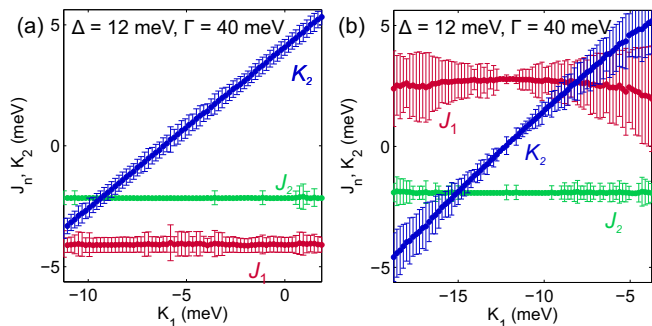


Figure S3. (Color online) Calculated parameters  $J_1$ ,  $J_2$ , and  $K_2$  as a function of  $K_1$ , showing results for both branches of solutions that met the conditions described in the article. (a) shows results for which  $J_1$  is antiferromagnetic, for which both  $J_1$  and  $J_2$  appear to be stable. Errorbars indicate the spread in each parameter calculated for each  $K_1$  starting point, as described in the text.

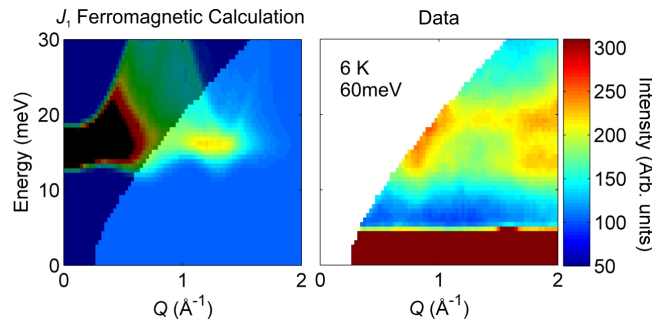


Figure S4. (Color online) Simulated powder-averaged spin-wave spectra for representative  $J_1$  ferromagnetic solution with calculated parameters  $K_1 = -5.6$ ,  $J_1 = 2.4$ ,  $J_2 = -1.9$ ,  $K_2 = 4.3$  meV. This is compared to data collected at  $T = 6$  K on SEQUOIA with  $E_i = 60$  meV. The shaded region in the calculations indicates the region of (Q,E) space which is inaccessible in the experimental set-up.

correction is applied to the resulting data, and the highest temperature point is then used to scale the saturated intensity to 1.

## SPIN-WAVE MODEL

For the calculation of the exchange parameters, the expression for the mean-field (MF) transition tempera-

ture is  $T_N = 2S(S+1)(3(J_2 + K_2) - 2(J_1 + K_1))/3$ . For different values of  $K_1$ , we estimate the possible range of the other parameters by their spread for given starting points. This parameter spread occurs because the problem is under-determined, which helps to avoid arriving at a local minimum. Even with  $K_1$  fixed, the coupled conditions for the stability of the ground state and for the spin-wave frequencies  $\Delta$  and  $\Gamma$  are insufficient to completely determine the remaining three parameters. Although  $\Delta$  and  $\Gamma$  depend only on the combination  $\kappa = 3K_2 - 2K_1$ , the errors in  $J_1$  and  $J_2$  affect the error in  $K_2$  for a fixed  $K_1$ . For both branches, however, the average value for  $\kappa$  is constant over most of the range of  $K_1$ , as seen in the linear relationship between  $K_1$  and  $K_2$ , Fig. S3.

Figure S3 shows the determined values of  $J_1$ ,  $J_2$ , and  $K_2$  for input  $K_1$  calculated using the constraints described in the main article (i.e.  $\Delta = 12$  meV and  $\Gamma = 40$  meV). Figure S3(a) shows the results for  $J_1$  antiferromagnetic, which produce an  $S(Q, E)$  which reasonably reproduces the data across the full range of  $K_1$ s as shown in the attached video D12\_G40\_AFM.mp4, and reproduced for representative values in the main article. The results with  $J_1$  ferromagnetic do not reproduce the observed neutron scattering results, as shown for a representative parameter set in Fig. S4 and additionally over the entire range of parameters in additionally the attached video D12\_G40\_FM.mp4. The  $\text{Os}^{5+}$  form factor from Ref. SM[1] was used for all simulations.

As a check to the validity of our results, we also tried our calculations for different values of  $\Gamma$  and  $\Delta$ . Here we show the calculated exchange parameters for  $\Delta = 12$  meV and  $\Gamma = 35$  meV, Fig. S5(a) and (b), and  $\Delta = 8$  meV and  $\Gamma = 40$  meV, Fig. S5(c) and (d). The resulting  $S(Q, E)$  from all of these cases as shown in videos D12\_G35\_AFM.mp4, D12\_G35\_FM.mp4, D8\_G40\_AFM.mp4 and D8\_G40\_FM.mp4, and none of the parameters reproduce the data like the  $\Delta = 12$  meV and  $\Gamma = 40$  meV results.

[1] K. Kobayashi, T. Nagao, and M. Ito, Acta Crystallographica Section A Foundations of Crystallography **67**, 473 (2011).

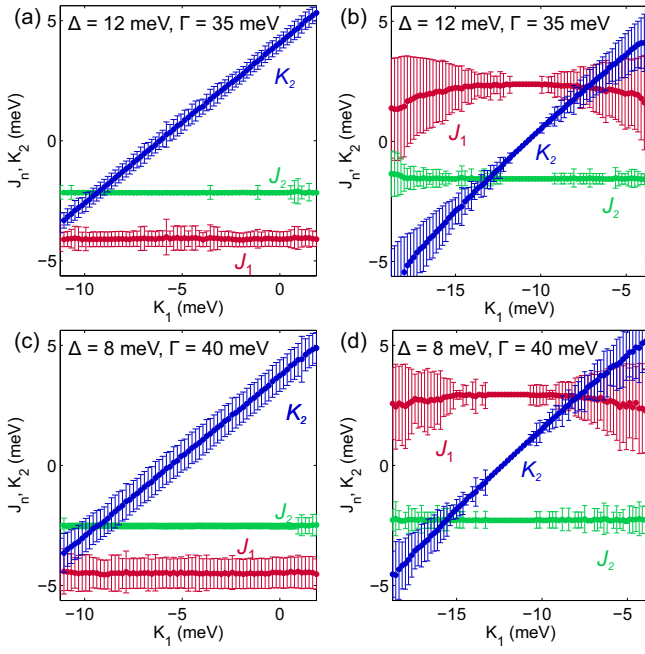


Figure S5. (Color online) Calculated parameters  $J_1$ ,  $J_2$ , and  $K_2$  as a function of  $K_1$ , for alternative values of  $\Gamma$  ((a) and (b)) and  $\Delta$  ((c) and (d)) showing results for both branches of solutions. Again the errorbars indicate the spread in each parameter calculated for each  $K_1$  starting point, as described in the text.